Repeat-pass Differential SAR Interferometry Applications to the San Rafael Glacier, Northern Patagonia Icefield, Chile.

ERIC RIGNOT
Jet Propulsion Laboratory, California Institute of Technology, Pasadena 91109, California, U.S.A.

RICHARD FORSTER AND BRYAN SACKS
Department of Geological Sciences, Cornell University, Ithaca 14853, New York, U.S.A.

ABSTRACT. One-day repeat-pass, Interferometric Synthetic-Aperture Radar data acquired in October 1994, at L-band frequency (24-cm wavelength), vertical transmit and receive polarization, by the Spaceborne imaging Radar-C were used to produce the first maps of both the surface topography and ice velocity of the north-western flank of the Northern Patagonia Icefield, in Chile. The topographic map has a 10-m horizontal resolution and a 10-m vertical resolution which should be sufficient to be used as a reference for future direct measurements of glacier mass changes. The ice velocity map, limited to one component of horizontal motion, provides estimates of daily motion in the line-of-sight of the radar with a precision of 5 mm. The results demonstrate the utilization of L-band SAR interferometry - and its possible superiority to C-band SAR interferometry - to monitor glaciological parameters on a spatial and temporal scale unattainable by any other means.

Over the San Rafael Glacier, a fast-moving, temperate, tidewater glacier with grounded terminus, the interferometric velocities, converted to two-dimensional displacements, reveal the presence of a 4.6 km-wide ice stream moving at 2.5 m/d from the central part of the icefield. Below the equilibrium line altitude, the ice stream moves at nearly the same speed until 5 km from the terminus where longitudinal stretching abruptly increases to very high values ($1\ a^{-1}$), initiating rapid flow which maintains throughout the terminal valley and yields terminal velocities > 17.5 m/d. Calculated resistive stresses show that longitudinal tension dominates the horizontal stress regime and that the initiation of fast flow at the entrance to the terminal valley is controlled by longitudinal gradients in longitudinal stress and by the driving shear stress.

Submitted to the Journal of **Glaciology**.

INTRODUCTION

The Southern and Northern Patagonia Icefields, in the southern part of South America, are the world's largest ice masses after the Greenland and Antarctic Ice Sheets (Warren and Sugden, 1993) (Figure 1). The Southern Patagonia Icefield .(Campo de Hielo Patagonico Sur) lies in the southern part of Chile and Argentina. at about 50° south and 73° west, and stretches along the southern Andes for 360 km, with a maximum width of 90 km. The Northern Patagonia Icefield (Campo de Hielo Patagonico Norte), centered at about 47° south, 73° 30" west, extends to lower latitudes than any 01 her ice mass, and covers a contiguous area of 4200 km^2, approximately 100 km long by 45 km wide. As the icefields are located in a zone of westerlies, the western part is wet with an estimated precipitation between 4,000 to 10,000 mm (Inoue *et al.*, 1987; Yamada, 1987), and the eastern part is dry (Ohata *et al.*, 1 985). Abundant, precipitation and high melt rates produce strep balance gradients, with a sharp cast-west contrast in glaciological characteristics. These highly contrasted dynamic glacial systems could offer many clues about northern and southern hemisphere asynchronous glacier behavior, calving dynamics, and mass-balance relationships, but their glaciological characteristics are poorly known. At present, topography exists for only a few glaciers, while no topography exist for the vast interior of the icefields. Velocity on both icefields has been measured on only five of the over 100 glaciers and these consist of only point measurements. Accumulation has been measured at only one location, and the mass balance of the icefields is unknown.

In this study, we discuss the application of the Synthetic-Aperture Radar (SAR) double difference interferometry technique to derive maps of both the surface topography and the ice velocity of the]]orth-western flank of the Northern Patagonian Ice field. The interferomet ric. SAR (InSAR) data were acquired in early October 1994 by the Spat.eborl]e Imaging Radar-C SAR on-board the space shuttle Endeavour, during the one-day exact repeat-l)ass cycle of its second mission, SRL-2. On October 8, 9, 10 and 11, four interferometric passes

and is diagonally traversed by the Liquine-Ofqui fault system ((1,14) to (45,1) in Figure 2). The fault scarp forms an abrupt mountain wall on the eastern side of the Laguna San Rafael, where surface elevation increases from sea-level to well-above 1400 m in less than 5 km.

The Sari Rafael Glacier is the most active glacier of the Northern Patagonia Icefield, draining 18% of its total area (Aniya, 1988). It is the lowest latitude tidewater glacier in the world. Its calving front is 30-70 m high, standing in water about 100-300 m deep, and therefore assumed to be grounded. Ice velocity exceeds 17-22 m/d (per day) near' its terminus (Kondo and Yamada, 1988), making the San Rafael Glacier one of the world's fastest glacier in a non-surge mode along-side with the Jakobshavn Isbrae in Greenland, a sub-polar tidewater glacier with floating terminus moving at 17-23 m/d (Echelmeyer and Harrison, 1990), and the Columbia glacier, Alaska, a temperate tidewater glacier with grounded terminus moving at 10-14 m/d (Krimmel and Vaughn, 1987; Walters and Dunlap, 1987; Meier and Post, 1987). The fast motion of the San Rafael Glacier probably results from a combination of factors that include the high accumulation rates recorded in the area (> 4000 mm per year), the steep western slope of the tectonically active mountains, the intense calving activity at the glacier terminus, and the warm climate which maintains warm ice temperatures, high rates of plastic ice deformation, and abundant subglacial water from melting and rainfall which should contribute to high rates of basal sliding (Naruse, 1985). The glacier is approximately 45 km long, 25 km wide in maximum, but confined to a 3 km-wide valley, 5 km from the terminus. Its total area is 780 km^2. The accumulation area is 585 km^2, the largest of the Northern Patagonia Icefield (Aniya ,1988), and 3.3 times the size of the ablation area. Accumulations rates are poorly known but may be the highest in the world since year-round rainfall and snowfall yield mean annual precipitation >8000 mm on the central plateau of the icefield (Escobar et al., 1992). Yamada (1 987) measured 3.54111 annual accumulation at 1290-m elevation from an ice core. Summer ablation varies from

6-7 cm/d near the terminus to 1-2 cm/d in the firn zone at 1000 m elevation (Ohata *et al.*, 1985; Kondo and Yamada, 1988). No data have been collected in winter. Warren (1 993) estimated summer calving fluxes to be about 2 Mm^3/a or 0.73 km^3/a (per annum), while Ohata *et al.* (1985) estimated that calving and melting contribute roughly equally to total mass loss. Aniya (1988) estimated the equilibrium line altitude to be at 1200 m. Ice thickness and bed topography are unknown. The only existing thickness estimates in the Northern Patagonia Icefield *were* obtained from gravity anomalies on Soler and Nef Glaciers on the eastern side, and along a transect joining the Nef Glacier to the accumulation area of the San Quintin Glacier in the central part of the icefield (Casassa, 1987). The San Rafael Glacier has been known to retreat at drastic rates of up to 300 m/a in the late 1980s, but glacial retreat halted in 1990, and the north margin advanced in 1991 and 1992 (Warren, 1993) while the southern margin retreated slightly (Wada and Aniya, 1 995). As typical of many other tidewater glaciers (Meier and Post, 1987), these fluctuations in position of the terminus do not reflect trends in air-temperature, but seem to follow annual changes in precipitation with a 5 to 10-year reaction time (Warren, 1993).

METHODS

Background.

The principles of SA R interferometry have been presented in scl'era] papers (e.g. Zebker and Goldstein, 1986; Goldstein *et al.*, 1988; Gabriel *et al.*, 1989; Zebker *et al.*, 1994a and 1994b), and recent applications over polar ice sheets have been discussed e.g. in Goldstein *et al.* (1993) for Antarctica and Rignot *et al.* (1995) for Greenland. Gabriel *et al.* (1989) introduced the double difference interferometry technique by which two successive SAR interferograms arc combined together to eliminate surface topography, leaving interferometric fringes solely related to small surface displacements consecutive to natural events such as an earthquake, a landslide, fault-creeping, ground-swelling, or ice motion. Here, wc describe the details relevant to the application of the double difference interferometry technique to

glacier studies, i.e. the inference of both surface topography and ice velocity of an icefield from a pair of SAR interferograms.

SAR interferometry exploits the phase coherence of radar returns received from reflecting surface elements by two slightly displaced radar antennas to measure the relative positions of those surface elements with great accuracy. These surface elements will appear displaced in the images collected by the two antennas as a result of two effects: 1) a "stereoscopic" effect due to slight, differences in viewing geometry of the surface elements by the two receiving antennas and to differences in surface elevation of the surface elements (Figure 3); and 2) actual motion of the surface elements in between the time of reception of the radar signals by the two receiving antennas if the antennas do not operate simultaneously (Figure 4).

When surface motion is negligible (e.g. the two antennas operate simultaneously), the "stereoscopic effect" is utilized to derive a topographic map of the imaged surface. The vertical accuracy in surface elevation is scaled by the baseline separation between the two receiving antennas and by the operating wavelength of the radar, but also depends on the phase noise level. Larger baselines produce more accurate surface elevations. Beyond a critical value of the baseline, however, the phase values decorrelate because the two antennas probe non-overlapping (hence independent) portions of the scattering patterns from the surface elements. This phenomena is called geometric decorrelation.

When surface motion is present, the surface displacements are detected in the line-of-sight of the radar within fractions of the radar wavelength (millimeters), independent of the baseline separation between the antennas, and far more precisely than with non-interferometric techniques which are typically limited by the size of the individual surface elements (tens of meters).

Repeat-track SAR interferometry is a particular mode of radar interferometry - used by the SIR-C/ C/X-SAR instrument - by which the same antenna is flown twice over the same area along almost the exact same trajectory. The baseline separation is determined by the

actual separation between successive flight tracks. Understandably, the baseline needs to be as short as possible to avoid geometric decorrelation effects, which requires well-maintained orbits. Direct advantages of the repeat-track interferometry include the greater simplicity of the instrument (only one antenna), the generation of more precise topography (possibility to synthesize larger baselines than those accommodated on a single platform), and the possibility to coherently detect surface changes. A major inconvenience is that the physical and structural properties of the surface elements may change in Detw'cell the two times of imaging, e.g. as a result of storm activity or snow/ice melt, in which case the distribution of scatterers is altered, temporal phase coherence is destroyed, and the InSAR technique is no longer applicable.

Generation of SAR **interferograms.**

The SIR-C/X-SAR instrument, as almost all existing mode] n SARs, recorded both amplitude and phase of the radar returns as I and Q quadrature components. The quadrature components were combined to form a complex number which represents the complex amplitude of the radar signal. '] 'he SIR-C images used here comprised 6292 range lines by 9592 azimuth lines of complex amplitudes, with a pixel spacing of 3.33 m in slant-range (corresponding to 4.5 m on the ground at a 43° incidence angle of the radar illumination) and 5.21 m in azimuth. To form an interferogram, the complex amplitudes from one data take (or image) were multiplied by the complex conjugate of tile complex amplitudes from a second data take. The interferometric phases were then computed as the argument of the cross-products. The cross-products were normalized by the signal intensity. Their magnitude therefore measured the temporal coherence of the interferometric phases between O (uncorrelated complex amplitudes or no phase coherence) and 1 (correlated amplitudes or complete coherence). '1'0 improve the phase signal. to-noise ratio, the cross-products were averaged together over several pixels before computing the phase, a process called "mult - looking", which is done at the expense of spatial resolution. We used 3 looks in range and

3 looks in azimuth, resulting in a 9-look interferogram. The process reduced phase noise and pixel size by 3. A larger number of looks would have further reduced phase noise but would have also destroyed interferometric details in regions of large strain rates such as the marginal shear zones of the San Rafael Glacier.

Prior to the computation of the cross-products, the two images had to be registered within sub-pixel accuracy. The mis-registration between images results from differences in clock-time bet ween successive passes (typically several pixels offset i n azimuth or along-track position), differences in viewing geometry due to the baseline separation (typically a range offset of fractions of a pixel), and non-parallel flights of the spacecraft (sub-pixel variations in bot h range and azimuth offsets). As phase coherence is sensit ive to sub-pixel registration errors (a displacement of two pixels results in a complete loss of phase coherence), the registration process must be very precise, It was done here using a correlation algorithm. The peak in correlation of the signal intensity (and not the complex amplitude) was searched within 16 pixels by 16 pixels windows at various image locations, interpolating the results to within 1/1 Oth of a pixel via Fourier transforms. The measured range and azimuth offsets were then fitted to a plane, i.e. the offsets were modeled to vary linearly as a function of pixel position in the 2-d plane.

Near the terminus of the San Rafael Glacier, this simple technique failed as the mis-registration of the images was also affected by the displacement of the glacier, which near the terminus exceeds one slant-range pixel per day. There, we applied the correlation algorith In to a large number of points, fitting the results throug h a non-planar surface that accounts for larger pixel displacements in the center-line of the glacier than on the side-margins. With this improved registration, wc obtained interferometric fringes for an additional 2-km segment of the terminal valley where no fringes were obtained using the simple plane-fitting technique. Fringes could however not be produced in the last 2-km segment preceding the calving front. Several reasons may explain the lack of phase coherence near the calving

front. First, spatial resolution is not sufficient at the margins to keep track of the very large transverse strain rates, i.e. phase values change by more than one cycle within a single pixel. Second, ice deformation is more severe, and rotation rates of ice blocks may exceed the 1.3° calculated theoretical limit beyond which phase coherence is destroyed at L-band based on the SIR-C SAR parameters and the study by Zebker and Villasenor (1992). ~'bird, surface melt is more likely to alter the distribution of scatterers as the glacier ice reaches sea-level and warmer air-temperatures. Finally, the glacier is severely crevassed near the terminus, with wide and extensive crevasses running across the entire glacier width. Over crevasse troughs, the radar returns are low - because of shadowing and close to the system thermal noise level, so phase noise is high and phase coherence is low. Over crevasse highs, the radar returns are bright but affected by specular reflections on the multiple facets of the seracs and layover of the geometry of the facets, so phase coherence is likely low there too. Hence, trains of large crevasses create large contiguous zones where phase noise is high.

Phase coherence (measured by the magnitude of the normalized cross-products) is shown in Figure 6a for the pair combining the data acquired on October 9 and 10, 1994 at L-band VV-polarization. Phase coherence is very high (> 0.95) in tile Laguna and in valley interiors, high over the icefield (<0.75), moderate (<0.'1) in areas of significant surface deformation (marginal shear zones), and low (< 0.2) over radar-dark areas (lagoon waters, surface lakes, river streams, and shadowed areas), pronounced ice deformation (icefalls near (43,19) and (48,17), and shear margins), or at very high elevation (at (46,20) in Figure 2). Above a certain altitude, we note a sharp decrease in correlation which, compared to hand-held photos taken by the astronauts on-board the shuttle, compares well with a transition from vegetated areas to snow-covered terrain with no vegetation (Rignot et al., 1996). Snow-covered bare areas are less correlated than vegetated areas. More importantly, the transition between the icefield and the rocky area is clearly visible as a sharp contrast in phase coherence across the entire icefield because rocks are more coherent than glacier

ice. This is not true in shadowed regions where phase coherence is lower on rocks, yet the discontinuity in phase coherence is still detectable. For comparison, the ice margin is difficult to identify in the radar amplitude images since rock and glacier ice have similar radar backscatter (Figure 2), and difficult to identify from optical imagery since snow-covered areas and ice are also not easily separated. This example suggest that phase coherence is a powerful tool for discriminating between different types of land cover and in particular for detecting the ice margin of an icefield.

The phase of the cross-products is a real number ambiguously wrapped between O and 2π that needs to be unwrapped to be converted into an absolute phase. To unwrap the phase values, we used the algorithm developed by Goldstein *et al.* (1988), which worked well in noise-free areas, but failed in areas of high phase noise, resulting in data gaps - in the best case - or unwrapping errors - in the worst, case. Unwrapping errors corresponded to blocks of contiguous pixels where phases were in error by a multiple of 2π compared to the surrounding phase values. These errors were manually corrected through a tedious and time-consuming process. Data gaps could not be corrected or filled in because they corresponded to areas where radar imaging is limited. Such was the case of mountain ranges where surface slopes exceeded the incidence angle of the radar illumination, resulting in shadowed regions (slopes away from the radar looking direction) of low signal-to-noise ratio, or layover regions (slopes facing the radar illumination) where radar ranging was ambiguous. Open water areas and crevasse troughs also yielded low coherence levels because of low signal-to-noise ratios (radar dark). Phases were however successfully unwrapped over the most part of the icefield.

Once the phases were unwrapped, we estimated the baseline parameters. As the shuttle ephemeris data were not known with the required degree of precision (< 1 m), the baseline

had to be estimated from the data. The phase difference between antenna 1 and 2 is

$$\phi_{21} = \frac{4\pi}{\lambda}[\, B_{21} \cos(\alpha_{21} + \theta_z) + V_r\, \delta t_{21} \,] + \phi_{21}^{o} \qquad (1)$$

where λ is the radar wavelength, B_{21} is the baseline separation between antenna 2 and 1, (Figure 3), α_{21} is the baseline angle with, horizontal, θ_z is the depression angle (a function of the surface topography z), V_r is the motion vector of ice in the line-of-sight of the radar (Figure 4), δt_{21} is the time lag between the two images, and ϕ_{21}^{o} is the absolute offset in phase. The angle θ_z is related to the slant-range distance r, the radar altitude H, the surface elevation z, and the earth's radius of curvature rt_0 (at nadir) and rt_1 (at the image center) by

$$\sin\theta_z = \frac{r^2 + (H + rt_0)^2 - (rt_1 + z)^2}{2\, r\,(H + rt_0)}. \qquad (2)$$

As both B_{21} and α_{21} varied along-track as successive paths of the spacecraft were not parallel, we estimated 5 baseline parameters from the data: B_{21}, α_{21}, their along-track gradients $\partial B_{21}/\partial y$ and $\partial \alpha_{21}/\partial y$, and the absolute phase offset, ϕ_{21}^{0}. For reference, r = 277.5 km, H = 215.3 km, rt_0 = 6367.40 km, rt_1 = 6367.42 km, and θ_z averaged 43°.

A few control points of known elevation were selected from the topographic maps of the Northern Patagonia Icefield published in 1982 by the Instituto Geographico Militar, in Chile, at a 1:50,000 scale, based on 1974-75 aerial photogrammetric mapping. The precision of the mapped surface elevation is unknown, and the ice!-cc)vcrccl area is completely blank due to the whiteness of the surface and the absence of image contrast in the aerial photos. We picked 50 tie-points outside of the icefield that could be identified in the radar images and for which phase coherence was high. As none of these control points were on glacier-ice, V_r = O in Eq. (l). The measured phases and image positions of the 50 control points were then used to solve for a system of 50 non-linear equations with 5 unknowns using the Levenberg-Marquardt method (Numerical Recipes, 1989). Although a smaller number of control points would have been sufficient to estimate the baseline parameters, using a larger

number of points further the estimation noise. The baseline results are shown in Table 1.

Surface Topography and Ice motion

Using the estimated baseline parameters in Table 1, we flattened the interferograms, i.e. removed the phase values corresponding to the imaging of a curved Earth as

$$\phi_{21,flat} = \frac{4\pi}{\lambda} [B_{21}(\cos (\alpha_{21} + \theta_z) - \cos (\alpha_{21} + \theta_0)) + V_r \delta t_{21}] \quad (3)$$

where θ_0 is the depression angle for flat terrain ($z = 0$ in Eq. (2)), and $\delta\theta_z = \theta_z - \theta_0$ is sufficiently small that $\sin \delta\theta_z \approx \delta\theta_z$. The advantage of removing the flat phase is that Equation (3) becomes a linear function of $\delta\theta_z$. With a second image pair, a system of two linearized equations is obtained

$$\phi_{21,flat} = \frac{4\pi}{\lambda} [B_{21} \delta\theta_z \sin (\alpha_{21} + \theta_0) + V_r \delta t_{21}] \quad (4)$$

$$\phi_{23,flat} = \frac{4\pi}{\lambda} [B_{23} \delta\theta_z \sin (\alpha_{23} + \theta_0) + V_r \delta t_{23}]$$

with two unknowns, V_r and $\delta\theta_z$. The time interval $\delta t_{21} = -\delta t_{23}$ was equal to one day. The surface elevation, z, was deduced from $\delta\theta_z$ using

$$z = \sqrt{r^2 + (rt_0 + H)^2 - 2 r (H + rt_0) \sin \theta_z} - rt_1 \quad (5)$$

To solve for Equation (4), two methods were possible. One method was to solve alternatively for V_r and $\delta\theta_z$ by multiplying the equations by the appropriate constants and linearly combined the equations. We selected another method which takes advantage of the fact that phases are a hundred times more sensitive to velocity than to topography (Eq. (1) and (2)). First, we solved for $\delta\theta_z$ through a linear combination of the two equations in Equation (4) and reported the result into the first equation. These $\delta\theta_z$ values were twice noisier than if they had been obtained from a single image pair because they resulted from double differencing of image pairs with similar but independent phase noise. The first equation was then solved for V_r, but since phases are a hundred times less sensitive to topography

than to velocity the solution was not affected by the noise of $\delta\theta_z$ and only depended on the phase noise of the first image pair. We then forced V_r to be zero over non-ice areas, to eliminate noise over those areas, reported the results into the first equation and solved this time for the topography term $\delta\theta_z$. The resulting values have a noise term equivalent to that of single differencing of the data. In addition, this method helped us verify that the baseline parameters were correctly estimated by comparing the two types of solution. Any error in one or both of the baseline parameters would have created distortions of the velocity field that would have been easy to detect. Comparing of the two solutions demonstrated that the baseline parameters were known very accurately and that the residual errors had no influence on the interferometric products.

The surface elevation and ice motion data were finally re-sampled from slaut-range geometry (the natural viewing geometry of tile radar) to ground-range geometry (more appropriate for georeferencing the data). The process depends on both the range distance to the radar and the surface elevation of each point. Resampling started from points further away from the radar along each range line, avoiding areas with no height information, and linearly interpolating in between positions for which a slant-range pixel fell directly into a ground-range pixel. Figure 5a shows the resulting false color composite image of the terrain topography, where huc and saturation are proportional to terrain height, and intensity is proportional to radar brightness at 1,-band. Figure 5b is a false color composite image of the surface motion in the radar looking direction (i.e. one component of ice velocity only), where intensity is proportional to radar brightness and color is proportional to ice velocity. Velocity is zero in non-glacier areas.

RESULTS AND DISCUSSION

L-band vs C-band Interferometry

Interferograms generated at C-band were much noisier than at L-band and did not yield useful glaciological products. The phase coherence of the C-band data acquired on October

9 and 10 is shown in Figure 6b for reference. Other C-band interferometric pairs yielded comparable or lower coherence levels than those shown in Figure 6b.

Coherence level s are expected to be lower at C-band than at L-band for several reasons. One reason is that errors in pointing angle of the radar antenna reduce phase coherence more significantly as the radar frequency increases. The along-track beamwidth of a radar antenna, which defines the zone over which radar signals are coherently detected, decreases in size with increasing frequency. For SIR-C, the antenna along-track beamwidth was 0.2° at C-band and 0.88° at 1,-band (wavelength ratio). 1 lence, the same error in pointing angle of the C- and 1,-band antennas resulted in a larger fraction of incoherent signals between the two data takes at C-band than it did at 1,-band. in fact 4.3 times larger.

We estimated the reduction in phase coherence of image pairs from pointing errors by calculating the pointing angle of the antennas during successive passes. Pointing angles scaled by the wavelength correspond to doppler frequencies in SAR processing. Doppler frequencies are typically estimated very precisely, here within 10-2011 z or an equivalent of 0.002-0.004°. Each data signal corresponds to a bandwidth-limited signal centered at the doppler frequency, with an along-track bandwidth equal to 950 Hz at both frequencies in the case of SIR-C. The doppler frequency at C-band is 4.3 times the doppler frequency at 1,-band (wavelength ratio). Since the SAR signals are bandwidth-limited, the reduction in phase coherence is simply calculated as the difference in doppler frequencies divided by the bandwidth. The results, shown in Table 2, indicate a reduction of common bandwidth of 2 to 9% at L-band compared to 9 to 38% at C-band. A further reduction in common bandwidth resulted from the fact that the two images forming a pair were processed at the same doppler frequency but not exactly at the average of the doppler frequencies from each data take. As a result, C-band coherence of one of the pairs was further reduced by 20'%. For the other pair, no further reduction in coherence resulted from the non-optimal selection of the processor doppler frequency. The difference in pointing angle was therefore

not sufficient to justify the observed lower coherence levels which cannot be due to system or processing effects and must be attributed to surface effects.

One surface effect is that C-band phases vary 4.3 t imcs (wavelength ratio) more rapidly than L-band phases for the same surface displacement. Spatial resolution being the same at the two frequencies, interferometric fringes "collapse" (which means phases vary by more than onc cycle within a single pixel) at C-band at lower rates of ice motion than at L-band. C-band interferometric fringes are naturally more rapidly destroyed in areas of high strain rates. For illustration, we multiplied the L-band phases by the wavelength ratio and observed that all fringes at the side-margins of the San Rafael Glacier collapsed. As a result, phase coherence will always be lower at C-band than at L-band in areas of high strain rates.

A second surface effect, probably the most significant in this case, is the difference in nature of the scat terers at the two frequencies. Radar penet ration increases with the radar wavelength, and radar signals interact preferabl y wit h objects comparable in size to the radar wavelength. Over the lagoon, where a dense temperate rainforest develops, C-band signals arc likely scattered by the upper and thinner tree branches and twigs of the forest canopy, whereas L-band signals seem to return mostly from the ground via double-bounce interactions of the radar signals on the tree-trunks (Rignot, E., 1996). From wind influence (known to be strong in that region), tree branches will be randoml y agitated, destroying C-band coherence from one day to the next, while leaving L-band signals undisturbed. A decrease of the coherence level of the vegetation is therefore expected as frequency increases. Similarly, over the icefield, 1,-band returns are expected to come from deep layers of snow/firn and ice and to be weakly affected by volume scattering from the fresh snow grains in the upper layers of the snow pack. C-band signals should inl.tract with the upper few centimeters of snow, especially in Patagonia where the snow water content is high passed a veneered layer of fresh snow (Yamada, 1987), and the large snow grains should efficiently scatter the C-band radar signal. Short-term environmental changes arc henceforth more

likely to affect the C-band radar returns from the surface than the L-band radar returns from deeper firn and ice (ice is a more stable medium than snow and firn).

In summary, the 1,- and C-band comparison suggests that L-band systems may offer a greater temporal stability of radar signals over glacial terrain and better chances of successful repeat-track SAR interferometry. In addition, L-band signals monitor larger strain rates and permit the detection of strain rates in deeper firn. Detection of strain rates at depth is more relevant because deep firn and ice are more likely to transmit the deep glacier stresses effectively to the surface than the more deformable upper medium of snow and firn. Monitoring of ice flow in deep firn should also reflect changes in ice discharge independent of short-term fluctuations in accumulation (Paterson, 1982).

An important question remains: to know at which depth L-band signals interact with the firn and how penetration varies with different physical properties of the snow and firn. Detailed comparisons between SAR-derived elevations, actual surface elevations and snow stratigraphy studies are required to answer that question. Such an investigation is currently underway in Greenland (Rignot and Bindschadler, unpublished floe.ulncnt, 1995), but no equivalent effort is envisioned in Patagonia. It is likely that the results will be different in a region where both snow/firn and ice are characterized by warmer temperatures (the mean air temperature is -6° C at 1290 m, even in the coldest months (Yamada, 1987)), meaning a larger snow/firn water content, more attenuation of the radar signals, and a greater reduction of their penetration depth. According to Yamada (1987), the mean minimum and maximum water content of the upper wet firn layer in the accumulation area of the San Rafael Glacier was 4 to 8% to a depth of 19.6 m. Using the mixing formula of Mätzler (1987)

$$\epsilon = \epsilon' + \epsilon'' = \epsilon_d + 23 * W / (1 - i f / f_o) \qquad (6)$$

where f_o is the relaxation frequency of wet snow (10 GHz) and ϵ_d is the dielectric constant

of dry snow, wc estimated the penetration depth, d_p, using

$$Cl_p = (\lambda \text{ fit'})) / (? \pi \epsilon") \quad (7)$$

with a snow density of 500 kg m^{-3} (Yamada, 1987) and $\epsilon_d = 1.97$ (Mätzler, 1987). We found d_p varying between 39 cm to 22 cm at C-band and 58 cm to 33 cm at 1,-band when W varied from 4% to 8%. Hence, even at 1,-band, radar signals are unlike] y to penetrate much deeper than probably 1 m in wet snow areas, which is smaller than the surface elevation noise (see below). Over bare ice, the penetration depth may be greater because the water content is close to 0% (Yamada, 1987). For impure ice at -5° C, Mätzler reported ϵ" of the order of 0.015 between L- and C-band, corresponding to a penetration depth of, respectively, 10 m to 60 m at C- and 1,-band. Ice temperature will however be lower in the ablation area which lays at elevation < 1000 m with average air temperature > 0°C even in the colder months (Inoue *et* al., 1987). Even a veneered layer of melted ice or large amounts of ice impurities carried by the glacier should suffice to drastically reduce penetration of the radar signals into bare ice compared to the abovementioned estimates. As a result, tile bias in surface elevation is again likely smaller than the r.m. s. noise in surface elevation ($\approx$ 10 m) and the bias in surface slope should be negligible.

Surface Topography.

The baseline value for the 157.8/1 73.8 pair was ten times larger than for the other pair, but the component of the baseline that is perpendicular to the line of sight of the radar, $B \sin(\theta_z + \alpha)$, which is the only one that matters for determining the precision in topographic height of the interferometry results, was similar for both image pairs and roughly equal to 40 m. This short value of the perpendicular baseline implied that the calculated height-to-phase noise ratio was 80 m/radians based on the formula in Zebker and Villasenor (1992) relating height noise to phase noise. Phase noise is determined by the signal-to-noise ratio, here equal to 13 dB on average over the glacier, resulting in a

phase noise of 0.2 radians. The height noise was therefore 18 m, further reduced by 3 by 3 multilooking to 6 m.

We verified these calculations by estimating the r.m.s noise level of the topographic height on various parts of the glacier of moderate inclination. We obtained a conservative estimate of the height noise equal to 10 m, consistent with the above calculated precision. Averaging of pixels overlarge areas will accordingly decrease the error by a factor sensibly equivalent to the square root of the number of averaged elements. The error should therefore decrease to only 1m over a 10 by 10 pixel area here corresponding to 156 m by 156 m surface elements.

No surface topography information had previously been obtained over that part of the icefield. As the San Rafael Glacier has been thinning (dramatically at a rate of about 10 m/a in the 1980's (e.g. Aniya, 1988), the SAR-derived topographic map is of sufficient accuracy to serve as a reference for monitoring long-term future mass changes of the icefield.

The inferred glacier topography is also immediately useful for estimating the surface slopes controlling glacial flow. As a rough figure, surface slope obtained from polynomial fitting and smoothing of the surface topography over 6 ice thicknesses was found to be constant at 3.5° at high elevation, increasing rapidly 5 km before the snout to reach 7.5° at the terminus (surface elevation was extrapolated between the lower portion of the interferogram and the calving front assuming a calving front at 70 m above mean-sea-level). Surface slopes are discussed in more details in the force-budget section.

Aniya (1988) estimated the ELA (Equilibrium Line Altitude) of the San Rafael Glacier at 1200 m from remote sensing data.. We did not find any evidence for changes in scattering behavior of the icefield at that elevation in the radar data. Complementary SIR-C data of the central part of the icefield however revealed a marked transition in radar backscatter at about 1300 m elevation, one kilometer beyond the edge of the interferometry scene (Rignot et al., 1996). The brighter signal below that boundary was attributed to interactions of the

radar signals with bare, rough and deformed ice, while the darker returns from the higher elevations probabl y resulted from interactions with a smooth, undeformed (the central part of the icefield is flatter) surface of wet snow and fi n. The observed transition in radar backscatter therefore occurred near the expected ELA but seemed more related to ice flow dynamics than to a transition in physical properties of the snow and firn.

Ice Motion.

Based on the r.m.s. noise of the velocity data, we estimated that the InSAR velocities of the San Rafael Glacier were known within 5 mm/d or 2 m/a. The calculated velocity noise is equal to $(\lambda/4\pi)$ times the phase noise, therefore. 3.8 mm when phase noise is 0.2 radians. Our above estimate of velocity noise from the data is therefore conservative. For comparison, estimates of glacial motion derived from feature trac king of crevasses in the lower reaches of the San Rafael Glacier are only known to within 1 m/d.

A number of striking features appear in the velocity map of Figure 5b. First, the data reveal the presence of an icc stream in the center portion of the San Rafael Glacier, manifest by an area of fast ice motion surrounded by slower moving ice and not by rock. One could argue that the icc stream is surrounded by several nunateks and is therefore not strickly speaking an icc stream, but the flow lines of the glacier visible in the shuttle photos indicate that the fast portion of the glacier is still active in the central part of the icefield (Rignot et a]., 1996) and is no longer surrounded by nunateks, therefore assimilable to an icc stream. At the margins, icc speed is not zero and icc is seen flowing into the streamy part of the glacier (purple color indicates motion away from the radar), feeding it from the interside mountain ridges, e.g. on the eastern of the glacier (at (31 ,17) and (28,15) in Figure 2). Second, the glacier seems to maintain its speed downslope until the last few kilometers of glacial flow where ice velocity suddenly increases dramatically. The large increase in speed occurs as the glacier enters the narrow terminal valley in a pattern of compressive ffow consistent with maintainance of ice discharge into the progressively narrower ice flow.

Finally, over the most part of the ice stream, the decrease in ice velocity is most pronounced at the shear margins and occurs over very short distances.

Icc velocities of other outlet glaciers arc much less than that for the San Rafael Glacier. The velocity of the Gualas Glacier, for instance, is largest at the higher elevations, but does not exceed 1 m/d, even though the glacier slope exceeds i'" *on* average (Aniya, 1988). Ice velocity decreases downflow to only several cm/d at its terminus, as is expected for an ablation glacier. Flow speed and flow evolution arc comparable for the Reicher Glacier. Both glaciers are connected to the central icefield through a series of ice falls, manifest in the radar data by a local loss of phase coherence, bright radar returns from a highly deformed surface, and a drop in SAR-derived elevations between the top and bottom portions of the suspected ice falls.

The InSAR velocities in Figure 5b provide only one component of horizontal motion. To get a full three-dimensional description of the velocity field, two additional interferometric pairs acquired at two different track angles would be necessary. If ice flow is assumed parallel to the ice surface, only one additional pair acquired at a different track angle is required instead of two. If, in addition, flow direction is known *a-priori* or assumed, then no additional interferometric pairs arc needed. in the present case, ice flows almost perpendicular to the flight track, which is the optimum configuration to detect principal ice motion in the radar looking direction, and flow direction may be assumed parallel to the ice stream margins as is usually the case for a valley glacier. We digitized the location of the boundary of the fast portion of the glacier, computed direction vectors along those boundaries, and interpolated the results in between the margins of streamy flow using 2-d cubic splines. The assumption of parallel flow should also be apl)lic.able since a maximum thinning rate of the glacier of 10 m/a yields a vertical component of motion of less than 2.7 cm/d whereas horizontal displacements in the center line of the San Rafael Glacier exceed 250 cm/d, i.e. a hundred times larger. The InSAR velocities, V_r, were thus converted into

ice velocities parallel to the surface, U, using (Figure 4)

$$U = V_r \; / \; [\cos\beta \cos\psi \sin\theta_i - \sin\beta \cos\theta_i] \tag{8}$$

where the surface slope β is counted positive downwards and obtained from the surface topography data. The local incidence angle θ_i is

$$\theta_i = \cos^{-1}\left[\frac{r^2 + (H + rt_o)^2 - (rt_1 + z)^2}{2\,r\,(rt_1 + z)}\right] \tag{9}$$

As surface slope was typically small, the conversion factor in Equation (8) is mostly determined by the value of the product $\cos\psi \sin\theta_i$. The resulting horizontal velocity (Figure 7) varies from 2.6 m/d near the ELA to > 12 m/cl in the lower reaches of the glacier. "Near the calving front, wc obtained estimates of horizontal motion by tracking crevasses between registered pairs of SAR amplitude images, using a cross-correlation technique similar to that used to register the complex amplitude images. We found that ice velocity reaches 17.5 m/d a fcw hundred meters from the calving front. These results confirm previous estimates of the enormous terminal velocity of the San Rafael Glacier (Naruse, 1985). They also reveal that the fast motion of the San Rafael Glacier is limited only to the 5-km long terminal valley. Elsewhere, ice velocity is quite large compared to that of other temperate glaciers, yet much less than the velocity at the calving front. The most striking feature remains the enormous increase in speed at 5 km which maintains throughout. the terminal valley. A similar pattern seems to exist on the Columbia Glacier, Alaska (Krimmel, 1992, Fig. 10, p. 14) where velocity increases from 3 m/d to greater than 10 m/d in about 7 km. The longitudinal stretching of the glacier is less than for the San Rafael Glacier and the transition is less spectacular, yet this flow behavior could be a fundamental characteristic of tidewater glaciers.

Ice Thickness

A transverse profile of the velocity near the ELA (1200 m), from (x,y) = (22.99,30.99) to (27.1 5.30.21) in Figure 2, is shown in Figure 8. The average velocity across the 4.6 km width

of the streamy part of the glacier is 2.17 m/d. To infer ice thickness from the velocity, we used a combined model of velocity due to basal sliding and velocity due to internal plastic deformation of the ice (e.g. Fastook *et* al., 1995). The component of motion due to internal deformation is

$$U_d = \frac{2}{n+1} \left[\frac{\tau_d}{A}\right]^n H \tag{10}$$

$$\tau_d = \rho\, g\, h \sin \beta$$

where τ_d is the driving stress, A is the column averaged flow constant for an ice column of thickness h, $\rho = 900\ kg\ m^{-3}$ is the ice density, and $g = 9.8\ m\ S^{-2}$ is the acceleration of gravity. For sliding, the general relationship for beds at the melting point developed by Weertman (1964) is

$$U_s = \left[\frac{\tau_d}{B}^m\right] \tag{11}$$

where B includes bed roughness and m is a visco-plastic parameter for sliding temperate basal ice. The column-averaged ice velocity is then a combination of the two models

$$U = f\, U_g + (1 - f)\, U_s \tag{12}$$

where f is the fraction of velocity due to sliding, taking values between O and 1. We used A = 200 kPa $a^{1/n}$ as this value is reasonable for temperate glaciers (Hooke, 1981; Weertman, 1 973) and $n = 3$. For sliding, we used B = 4 kl'a $a^{1/m}$ and $m = 2$ (Fastook *et al.,* 1995). The results suggested that internal deformation alone ($f = O$) could not explain the observed velocities as the resulting thickness of 560 m would yield a driving stress of 305 kPa, which is extremely large and unlikely (Paterson, 1 981). Conversely, pure basal sliding ($f = 1$) yielded an ice thickness of 230 m, probably underpredicted, and pure basal sliding is unlikely to dominate in the accumulation area of a glacier. More reasonable results were obtained with $f = 0.3$. The estimated maximum ice thickness was $h = 385$ m, corresponding to a driving stress $\tau_d = 210$ kPa at the center-line, decreasing towards

the margins. The resulting basal velocities were equal to 84% of the surface values along the center-line, which seems realistic given the rates of sliding of other temperate glaciers (Paterson, 1982, p. 71) and assuming that glacier sliding is even more significant for low latitude Patagonian ice.

Multiplying the estimated glacier cross-section (assuming flat bottom and vertical walls) with the mean velocity along the transverse profile yielded an ice flux of 1.4 km^3/a. For comparison, summer calving fluxes were estimated by Warren (1993) to be about 0.73 km^3/a, and ice ablation was estimated to be of the same order of magnitude by Ohata et al. (1985). The sum of ablation and calving is therefore about 1.5 km^3/a in the summer and the yearly average should be lower. No winter data on ablation and calving rates exist for the San Rafael Glacier. Calving and ablation combined together seem however to first order to balance ice discharge from the accumulation area.

Applied to the entire accumulation area of the San Rafael Glacier, the ice discharge would balance accumulation if accumulation averaged 2.4 m/a over the entire icefield. Accumulation was 3.54 m according to Yamada (1987) at 1290 m elevation. This value is higher than the steady-state average accumulation but this is a reasonable result since the drilling site used by Yamada laid directly in the path of the westerlies from the Pacific, unprotected by high mountain walls, and therefore likely exposed to higher-than-average accumulation rates.

Estimating ice discharge at lower elevations would have been a more difficult exercise for the San Rafael Glacier because basal sliding is likely to dominate and B is not a well-known parameter. In addition, intense glacier crevassing probably reduces the mean density of ice to an unknown much lower value since the glacier is heavily crevassed near the calving front, with large and widely spaced crevasses.

Force Balance

An important advantage of the InSAR technique is to provide naturally gridded ve-

locities, and more importantly to obtain direct observations of differential ice motion, i.e. strain rates. Strain rates are more relevant - and more difficult to measure in the field or to calculate from point measurement velocities - to glacier studies that absolute velocities because they are necessary to interpret borehole deformation (Paterson, 1982), but also because they directly intervene in the force-budget of the glacier as strain rates are related to deviatoric and then resistive stresses through the flow law of ice. Here, we used the InSAR velocities corrected for flow direction to estimate the strain rates, and thereon calculated the stresses acting on the glacier. The x- and y-components of the velocity were obtained from Eq. (8) using

$$u_x = U \cos(\beta) \cos(\psi) \tag{13}$$
$$u_y = U \cos(\beta) \sin(\psi)$$

The longitudinal and transverse components of the velocity were deduced as

$$u_L = u_x \cos(\psi_{cent}) + u_y \sin(\psi_{cent}) \tag{14}$$
$$u_T = -u_x \sin(\psi_{cent}) + u_y \cos(\psi_{cent})$$

where ψ_{cent} is the average flow direction computed along the center-line, which defines the direction of the longitudinal axis, L. Surface strain rates were computed using central differencing as

$$\dot{\epsilon}_{ij} = \frac{1}{2}\left(\frac{\partial u_i}{\partial j} + \frac{\partial u_j}{\partial i}\right), \quad \{i,j\} \in \{L,T\} \tag{15}$$
$$\dot{\epsilon}_{ZZ} = -(\dot{\epsilon}_{LL} + \dot{\epsilon}_{TT})$$
$$\dot{\epsilon}_e^2 = \frac{1}{2}\dot{\epsilon}_{ij}\dot{\epsilon}_{ij}$$

where the last equation expresses the conservation of ice volume, and $\dot{\epsilon}_{ZL} = \dot{\epsilon}_{ZT} = 0$.

The effective strain-rate, $\dot{\epsilon}_e$, shown in Figure 9, is ten times larger near the margin than in the center and is dominated by lateral shear. This means that ice is softening at the

margins of the ice stream, resulting in a decoupling of the ice stream from the rest of the glacier ice, thereby maintaining rapid flow. Along the center-line $\dot{\epsilon}_e$ is 0.15 a^{-1} at 1200-m elevation, increasing to 1 a^{-1} in the 2.5-km wide and 5-km long terminal valley. This large longitudinal gradient along the center-line is not due to lateral shear but to an increase in longitudinal stretching of the glacier in the terminal valley where more rapid flow develops.

The surface strain rates were in turn used to calculate the deviatoric and then resistive stresses acting on the glacier following Van der Veen and Whillans (1989). Expressed in terms of strain rates, the resistive stresses are

$$R_{ii} = A\,\dot{\epsilon}_e^{\frac{1}{n}-1}\,(2\,\epsilon_{ii} + \epsilon_{jj}) \tag{16}$$

$$R_{ij} = A\,\dot{\epsilon}_e^{\frac{1}{n}-1}\,\epsilon_{ij}, \qquad \{\,i,\,j\,\} \in \{\,L,\,T\,\}$$

The results are shown in Figure 10. The normal stresses, R_{LL} and R_{TT}, *show* much more variability than the shear stress, R_{LT}. The shear stress varies relatively uniformly between -150 kPa and +-150 kPa across the glacier width, corresponding to a nearly constant lateral drag of 150 kPa. Considering that the width of the ice stream (4.6 km) is]2 times its calculated thickness (385 m), the total lateral drag applied on the edges of the ice stream must only represent a small fraction of the total resistive force on the ice stream. The ratio of the total lateral resistive force to total gravitational driving force is very low and also independent of our calculated glacier thickness. We conclude that the margins do not play a strong role in the resistive control of the San Rafael Glacier. This results is in contrast to active ice streams in Antarctica where resistive drag is equally partitioned between the margins and the bed (Echelmeyer et al., 1994)

Longitudinal tension, R_{LL}, varies between -250 kPa and +250 kPa above the terminal valley but reaches 300 kPa in the terminal valley. The feature tracking results suggest longitudinal tension should remain high in the terminal valley since the longitudinal strain rate remains > 1 a^{-1} (Figure 7). The transverse stress, R_{TT}, shows similar spatial variations,

yet typically less than 150 kPa in magnitude. Longitudinal tension therefore dominates the horizontal stress regime, with large local variations, and very high values in the terminal valley.

To determine the pattern of basal friction, we used the isothermal block flow approach of Van der Veen and Whillans (1989), neglecting bridging effects. The longitudinal basal drag, $\tau_{b,L}$ is estimated from the longitudinal driving Stress, $\tau_{d,L}$, and the vertically-avel"agc:(l gradients in longitudinal and transverse stresses using the relation

$$\tau_{b,L} = \tau_{d,L} - h\frac{\partial R_{LL}}{\partial L} - \gamma\, h\frac{\partial R_{LT}}{\partial T} \qquad (17)$$

where h is the ice thickness, ancl R_{LL} and R_{LT} are vertically-averaged stresses here chosen equal to their value at the surface and abusively noted with the same notation as for the surface stresses. γ is a "fudge" factor between O and l that we introduced to account for the decrease in ice hardness with increasing depth, assuming that strain rates remain depth-independent. γ could actually be a complicated function of ice hardness, basal shear stress and other strain rates in the ice column. Its value is unknown but must be less than one to maintain depth-averaged gradients lower than their value at the surface. With $\gamma = 1$, we obtained largely negative basal drags in several places, an impossible result. The failure of this calculation is due to the fact that surface gradients in horizontal stress arc much larger than depth-averaged gradients. To obtain positive basal drag, γ needed to be lower than 1 /2. The isothermal block flow approach of Van der Veen and Whillans (1989) therefore overestimates the depth-averaged gradients in horizontal stress by a factor > 2.

Pursuing the calculation with $\gamma = 1/2$, we computed the driving stress using an ice thickness varying linearly between 385 m at 1200 m elevation and 280 m at the calving front (the lagoon waters near the calving front are 200 m deep on average at the center line and the ice cliff is about 80 m above sea level). Surface slopes were smoothed using a "triangular" window 3 ice thicknesses in size (1.2 km). "Triangular" here means that

the averaging coefficient was a decreasing linear function of the distance to the center point where smoothing was performed. The size of the window was selected based on the calculations by Kamb and Echelmeyer (1 986), in particular their Eq. (23) and (1 9) with u_o = 5 in/d, h =385 m, τ_b = 210 kPa, and n = 3, which indicate a longitudinal coupling length of 1.2 km. The resulting maps of driving stress, longitudinal gradients in longitudinal tension, and basal friction are shown in Figure 11. The different components of Equation (17) are compared in Figure 12 along the cm,ter-line of the glacier.

The transverse gradients in shear stress (not shown in Figure 11) are typically much lower than the longitudinal gradients in longitudinal stress and have therefore a second-order effect on the resisti vc drag to ice flow. Both the driving stress and the longitudinal gradients in R_{LL} vary with a dominant I-2 km wavelength, equivalent to 3-4 ice thicknesses, Similar variations in surface slope and driving stress have been observed on many glaciers, with a dominant wavelength of 3.3 times the ice thickness (Paterson, 1982, p. 167). Upstream from the terminal valley, maximum gradients in R_{LL} usually coincide with a rapidly decreasing driving stress, and large negative gradients correspond to areas of rapidly increasing driving stress. This trend is consistent with icc flowing over basal highs or areas of greater basal friction where compressive flow develops upstream from the basal highs and extensive flow takes place downstream from the basal highs (e.g. Whillans and Jezek, 1987), perhaps enhanced by the fact that ice is softer in Patagonia than in polar regions. Variations in surface slope therefore explain the major features of the velocity pattern and basal drag is dominantly controlled by the driving stress, yet with a non-negligible modulation in amplitude by longitudinal gradients in longitudinal stress.

The force-budget changes significantly in the terminal valley, or more precisely 5.1 km from the terminus (tile terminal valley starts at 4.5 km) at the initiation of more rapid flow. The transition is marked by a rapid increase in longitudinal tension R_{LL}, yielding a peak in the R_{LL} gradient > 300 kPa (Figure 11). A fcw hundred meters before that

transition, the driving stress increases from 50 to 200 kl'a due to an increase in surface slope. Basal drag is > 300 kPa, the highest of the whole profile. The other locations where basal drag and R_{LL} gradients are both large are at 8 km and 9 km where a slow-moving tributary y glacier joins the main flow of the San Rafael Glacier from the south (Figure 2) in an almost perpendicular direction. in the terminal valley, the R_{LL} gradients are dominantly negative, further decreasing downflow, thereby indicating a stronger counter-balancing of the driving stress and much lower levels of basal resi stance. The extrema in R_{LL} do not coincide as clearly with extrema in driving stress. We conclude that in that portion of the flow the variations in surface slope do not fully explain the velocity pattern. Gradients in longitudinal stress play a more significant role in balancing basal friction and driving stress, and basal friction varies in a more complicated fashion than indicated from surface slopes. Basal friction is 200 kPa at sites separated by 1 km, lower on average than upstream, perhaps a result of enhanced basal sliding. The effect of lateral drag is unclear because the interferometry data do not extend to the margins of the glacier where lateral drag is the largest. 'l'he glacier width remains however sufficiently large compared to its thickness and the driving stress is still sufficiently high that lateral drag probably still does not provide strong resistance to glacier flow compared to basal d rag, although the difference between the two is probably decreasing downslope.

in summary, these first-order calculations, based on measurements at the surface of the glacier, suggest that the initiation and maintainance of rapid flow of the San Rafael Glacier is controlled by both longitudinal gradients in normal stress and by the driving stress. Longitudinal gradients in normal stress are probably influenced by the geometry of the glacier. The maintainance of ice discharge through a narrower channel section (by almost a factor of 2) must partial] y explain the pattern of com pressive flow observed at the entrance to the terminal valley. At the same location, surface slope also increases by several degrees, indicating a coincident increase in driving stress. These two factors must play a significant

role in the initiation of fast flow.

A great unknown remains the role of water pressure at the bed. As for other tidewater glaciers, sub-glacial water must play a central role in the initiation and progression of rapid flow, especially in the case of a low latitude glacier where surface melting is considerable. A decrease in effective pressure at the bed has tremendous influence on basal sliding and has been identified as the prime cause for the rapid flow of tidewater glaciers (Meier and Post, 1987). Long term extensive studies of the Columbia Glacier, Alaska, (Kamb et al., 1994; Meier et al., 1994) recently confirmed that high glacial flow is mainly due to rapid basal sliding caused by high water pressure. As the glacier bed reaches sca-level elevation, the effective water pressure drops to zero, yielding high basal sliding velocities. Whether high basal water pressure fully explains the spectacular ice velocity pattern exhibited by the San Rafael Glacier is unknown from the interferometry data. In- situ observations of the glacier bed geometry, ice thickness, bed conditions, and hydrological variables would clearly help address that issue. Perhaps sub-glacial water is nat u rally channeled toward the entrance to the terminal valley at the location where fast flow initiates, creating a local increase in basal water pressure, fixed in space by the particular glacier bed geometry, and triggering high basal sliding and rapid ice flow. Part of the San Rafael Glacier bed could also reach sea-level at that location. 1)etermining where the glacier bed goes below sca-level would help estimate the decrease in basal water pressure and predict its effect on basal sliding. Although SAR interferometry data do not provide any information about these deep processes crucial to the detailed understanding of fast flow mechanisms, they clearly indicate in a unique and comprehensive fashion where on the San Rafael Glacier detailed field work should be conducted and w'here it should be most effective and useful to understand the dynamics of its rapid flow better.

CONCLUS1ONS

L- band SA R interferometry provides glaciological parameters on a temporal and spatial

scale unachievable by any other means. In this study, wc demonstrated the retrieval of' both surface topography and ice velocity over a poorly unknown portion of the Northern Patagonia Icefield using pairs of SAR images collected by the SIR-C/X-SAR instrument. The greater temporal stability of the 1,-band radar returns from the icefield compared to that obtained at C-band suggests that L-band systems should be of greater and more reliable usc to the glaciological community than C-band systems (the success rate of which was 0/4 in this study against an almost 4/4 for L-band). L-band signals should also permit the detection and monitoring of larger strain rates, at greater depth, therefore less dependent on environmental forcing and short-term fluctuations in snow accumulation. ERS-1 SAR is currently the only SAR system that could be used to continue and complete the mapping and monitoring of the Patagonian Icefields, but it operates a C-band system.

The topographic information provided by the SIR-C/X-SAR double difference technique has a 10-m precision in height, which should be sufficient for monitoring mass changes of the icefield over a period of several years. The detection of sur face changes caused by ice motion is far more accurate since its precision exceeds 5 mm/d, and strain rates are obtained directly from the InSAR measurements.

The lnSA R results of the San Rafael Glacier confirmed the very high ice velocity and longitudinal stretching of this temperate, tidewater glacier, but added a few new key features. The data revealed the presence of an ice stream in the c.enter part of the San Rafael Glacier that probably initiates very deep inside its accumulation area. Ice velocity is already large at 1200 m elevation compared to most temperate glaciers, but it increases even more dramatically 5 km from the calving front as the glacier enters the terminal valley. This increase in velocity could be a characteristic feature of tidewater glacier, although it may be emphasized on tile San Rafael Glacier because of the Patagonian climatic conditions. Calculated stresses acting on the glacier reveal that the initiation of rapid flow is controlled by longitudinal gradients in normal stress and by the driving stress as for other tidewater

glaciers. More detailed measurements and complementary studies of the glacier conditions below the surface - guided by the SAR interferometry data - are however necessary to provide indispensable information on ice thickness, bed geometry, bed conditions, and basal sliding to understand in a more complete fashion the transition to streamy flow, its controls and its long-term stability.

ACKNOWLEDGEMENTS. This work was performed at the Jet Propulsion Laboratory, California Institute of Technology, under a contract, with NASA's Polar Research Program and as part of the S1 R-C Science Project. We would like to thank the people at the Jet Propulsion Laboratory that processed the SI it-C/X- SAR data into complex amplitude products, and Drs. Charlie Werner and Paul Rosen for sharing their implementation of the phase unwrapping program. We would also like to thank Barclay Kamb and Hermann Engelhardt for useful discussions near the completion of this manuscript on the relevance of these results to studies of rapid glacial flow, and in particular to that of the Columbia Glacier, Alaska.

REFERENCES

Aniya M. 1988. Glacier inventory for the Northern Patagonia Icefield, Chile, and variations 1944/45 to 1985/86, *Arctic and Alpine Research* **20**(2), *179-187* .

Aniya M. and H. Enomoto. 1986. Glacier variations and their causes in the Northern Patagonia Icefield, Chile, since 1944, *Arctic and Alpine Research* 18(3), 307-316.

Bentley, C. It. 1987. Antarctic ice streams: a review, *J. Geophys. Res. 92(119), 8843-8858.*

Casassa G. 1987. Ice thickness deduced from gravity anomalies on Soler Glacier, Nef Glacier and the Northern Patagonia icefield, *Bull. Glacier Res.* 4, 43-57.

Echelmeyer, K. and W.]). Harrison. 1990. Jakobshavn Isbrae, West Greenland: seasonal variations in velocity- - or lack thereof, *J. Glaciol.*, **36** (122), 82-88.

Echelmeyer, K., W.]). Harrison, C. Larsen and J.E. Mitchell. 1994. The role of the margins in the dynamics of an active ice stream, *J. Glaciol.*, **40**, 136, 527-53S.

Escobar, F., 1{'. Vidal, C. Garin and R. Naruse. 1992. Water balance in the Patagonia Icefield. *In* Naruse, R. and Aniya, M. (eds), *Glaciological Researches in Patagonia, 1990.* Japanese Society of Snow and Ice, 109-119.

Fastook, J.I,., Il. H. Brecher and T. J. Hughes 1995. Derived bedrock elevations, strain rates and stresses from measured surface elevations and velocities: Jakobshavn Isbrae, Greenland, *J. Glaciol.* 41(137), 161-1'73.

Gabriel, A. K., R.M. Goldstein and H.A. Zebker. 1989. Mapping small elevation changes over large areas: differential radar interferometry, *J. Geophys. Res.* '34(117), {)183-9191.

Goldstein, R. M., 11. A. Zebker and C. I,. Werner. 1988. Satellite radar interferometry: two-dimensional phase unwrapping, *Radio Science*, 23, 713-720.

Goldstein, R. M., 11. Engelhardt, B. Kamb, and R. Frolich. 1993. Satellite radar interferometry for monitoring ice sheet motion: application to an Antarctic ice stream, *Science*, **262**, 1525-1530.

Harbor J. M. 1992. Application of a general sliding law to simulating flow in a glacicr cross-section, *J. Glaciol.* 38(128), 182-190.

Hooke, R. LeB., 1981, Flow law for polycrystalline ice in glaciers: comparison of theoretical predictions, laboratory data, and field measurements, *Rev. Geophys. Space Phys.* 19(4), 664-672.

Inoue, J., 11. Kondo, Y. Fujiyoshi, Y. Yamada, 11. Fukami and C. Nakajima. 1987. Summer climate of the Northern Patagonia Icefield, *Bull. Glacier Res.*, **4**, 1-14.

Kamb, B. and 5 others. 1994. Mechanical and hydrologic basis for the rapid motion of a large tidewater glacier 2. Interpretation. *J. Geophys. Res.*, **99**, b8, 15,231-15,244,
Kondo, H and T. Yamada. 1988. Some remarks on the mass balance and the terlninal-lateral fluctuations of San Rafael Glacier, the Northern Patagonia Icefield, *Bull. of Glacier Res.* **6**, *55-63.*

Krimmel R.M. and B.H. Vaughn, 1987, Columbia Glacier, Alaska: changes in velocity 197 7-1986, *J.*

Geophys. Res. 92(139),8961-8968.

Krimmel, R.M. 1992. Photogrammetric determination of surface altitude, velocity, and calving rate of Columbia Glacier, Alaska, 1983-91, *U.S. Geol. Surv. Open File Rep.*, 92-104.

Lliboutry, L. 1956. *Nieves y Glaciares de Chile: Fundamentos de Glaciologica.* Santiago: Universidad de Chile, 471 pp.

Naruse, R. 1985. Flow of Soler Glacier and San Rafael Glacier, in Nakajima, C. (ed), *Glaciological Studies in Patagonia Northern Icefield, 1983-1984.* Data Center for Glacier Research, Japanese Society of Snow and Ice, 64-69.

Ohata, T., H. Kondo and H. Enomoto. 1985. Characteristics of ablation at San Rafael Glacier, *In* Nakajima, C. (cd), *Glaciological Studies in Patagonia Northern Icefield, 1983-1984.* Data Center for Glacier Research, Japanese Society of Snow and Ice, 37-45.

Mätzler, 1987, Applications of the interaction of microwaves with the natural snow cover, Rem, *Sens. Rev.* 2(2),259-387.

Meier, M.F. and A. Post. 1987. Fast tidewater-glaciers, *J Geophys. Res.* 92(119), 9051-9058.

Meier, M.F. and 10 others. 1994. Mechanical and hydrologic basis for the rapid motion of a large tidewater glacier 1. observations. *J. Geophys. Res.*, **99**, b8, 15,21915,229.

Paterson, W. S. J]. 1982 *The physics of glaciers, Second Edition.* Oxford, etc., Pergamon Press.

Rignot, E., K. Jezek and H. G. Sohn. 1995. Ice flow dynamics of the Greenland Ice Sheet from SAR Interferometry, *Geophys. Res. Lett.* 22(5),575-578.

Rignot, E., R. Forster, and B. Isacks .1996. Mapping of Glacial Motion and Surface Topography of Four Outlet Glaciers of the Northern Patagonia Icefield, Chile, using Satellite SAR Interferometry Data. 1996. *Annals of Glaciology*, Special Issue EISMINT Meeting, Chamonix, Sept. 18-22 1995, France, in review.

Rignot, E., SIR-C SAR Interferometry Studies of Tropical Rain forests: 1,- and C-band comparson, in preparation, 1996.

Van der Veen, C.J. and I.M. Whillans. 1989. Force budget: I. Theory and numerical methods, *J. Glaciol.* 35(119),53-60.

Wada, Y. and M. Aniya. 1995. Glacier variations in the Northern Patagonia Icefield between 1990/91 and 1993/94, *Bull. Glacier Res.* 13, 11)-1 19,

Walters, R.A. and W.W. Dunlap. 1987. Analysis of time series of glacier speed: Columbia Glacier, Alaska, *J. Geophys. Res.* **92**(B9), 8969-8975,

Warren C. R.. 1993. Rapid recent fluctuations of the calving San Rafael Glacier, Chilean Patagonia: climatic or non-climatic? *Geografiska Annaler* **75** A, 111-125.

Warren C. R. and D. E. Sugden. 1993. The Patagonian Icefields: a glaciological review, *Arctic and Alpine Res.* **25**(4), *316--331.*

Whillans, I.M. and K. Jezek. 1987. Folding in the Greenland Ice Sheet, *J. Geophys. Res.* 92, 485-493.

Weertman, J. 1973. Creep of ice. *In* Whalley, E., S.J. Jones and L.W. Gold, *eds. Physics and chemistry of* ice. Ottawa, Royal Society of Canada, 320-337.

Weertman, J. 1964. The theory of glacial sliding, *J. Glaciol.* 539), 287-303

Yamada T. 1987. Glaciological characteristics revealed by 37.6 m deep core drilled at the accumulation area of San Rafael Glacier, the Northern Patagonia Icefield, *Bull. Glacier Res.* 4, 59-67.

Zebker, 11. A. and R.M. Goldstein. 1986. Topographic mapping from interferometric SAR observations, *J. Geophys. Res.* **91** (B5), 4993-4999.

Zebker, H .A. and J. Villasenor. 1992. Decorrelation in interferometric radar echoes, *IEEE Trans. on Geosc. and Rem. Sens.* 30 (5), 950-959.

Zebker, H.A., C.],. Werner, P.A. Rosen and S. Hensley. 1994a. Accuracy of topographic maps derived from ERS-1 interferometric radar, *IEEE Trans. Geo sc. and Rem. Sens.* 32, 823-836.

Zebker, H.A., P. A. Rosen, R.M. Goldstein, C. Werner and A. Gabriel. 1994b. On the derivation of coseismic displacement fields using differential radar interferometry: the Landers Earthquake, *J. Geophys. Res.* 99(1110), 19,617-19,634.

LIST OF FIGURES

Figure 1. Location map of the study area with inset showing the location the San Rafael Glacier, Northern Patagonia Icefield, in Chile.

Figure 2. False-color composite image of tile San Rafael Glacier in slant-range geometry acquired by the SIR-C/X-SAR instrument on October 10, 1994. The y-axis corresponds to the azimuth (along-track) direction, the x-axis to the slant-range direction. Kilometer units refer to the (x,y) positions mentioned in the text. The Silt-C/X-SAI{ instrument flew from left to right, with near-range on top, looking to its right. The scene corresponds to an illuminated area about 50 km x 33 km in size on the ground.

Figure 3. imaging geometry of the SAR interferometer defining the depression angle θ, the baseline angle α_{21}, the baseline distance B_{21}, the Earth radius of curvature at nadir, rt_0, and at the scene center, rt_1, the altitude of the SAR platform 11, the surface elevation z and the range distance r.

Figure 4. Geometry of imaging of the iCC flow, showing the velocity component measured along the line-of-sight of the radar (thick line), the slope angle β, the flow direction ψ, the depression angle θ_z, the local incidence angle θ_i, and the flow vector U (dotted thick line).

Figure 5. (a) Color-composite image of the surface topography of the Laguna San Rafael, Chile, in ground-range geometry. (b) Color-composite image of ice motion in the radar-locking direction. Unknown topography resulting from low phase noise was filled in by bilinear interpolation wherever possible, i.e. for small regions (10-30 pixels wide) or areas of low surface slopes (terminus of the San Rafael Glacier). Ice motion away from the radar direction (< - 6 cm per day) is colored purple. Low ice motion (< $\pm$ 6 cm per day) is colored blue. Large ice motion toward the radar direction is color coded light blue (6 to 20 cm pcr day), green (20 to 45 cm per day), yellow (45 to 85 cm per day), orange (85 to 180 cm pcr day), and red (> 180 cm per day). Non-glacier areas arc represented in grey scale based on the radar brightness of the terrain, Color saturation over the icefield is modulated by radar brightness.

Figure 6. Phase coherence image of the Laguna San Rafael, Chile at (a) L-band frequency, vertical transmit and receive polarization; (b) C-band frequency, vertical receive and transmit polarization. Bright areas are higly correlated vei sus dark areas where phase coherence is low.

Figure 7. Ice velocity and surface topography along tile center-]illc of the San Rafael Glacier as a function of distance to the calving front . Additional velocity measurements (squares) obtained from feature tracking are also shown near the terminus to complete - and in one place overlap - the interferometric measurements.

Figure 8. Transverse profile of the surface velocity of the San Rafael Glacier at 1200 m (equilibrium line altitude).

Figure 9. Effective strain rate, ϵ_e at surface, along the fast portion of the San Rafael Glacier,

Figure 10. (a) Longitudinal resistive stress, R_{LL}, at surface, (b) Horizontal shear resistive stress, R_{LT}, at surface, (c) Transverse resistive stress, R_{TT} at surface, of the San Rafael Glacier.

Figure 11. (a) Driving stress, τ_{dL}; (b) Integrated longitudinal gradients in longitudinal stress, $\partial H R_{LL}/\partial L$; and (c) Basal drag, τ_{BL}, of the San Rafael Glacier.

Figure]2. Driving stress, τ_{dL}, (continuous thick line), Basal drag τ_{BL} (long-dotted thick line), integrated longitudinal gradients in longitudinal stress 13111{1,1,//)1, (continuous line), and integrated transverse gradients in shear stress $\partial H R_{LT}/\partial T$ (dotted thin line) along the center-line of the San Rafael Glacier versus the distance to the calving front.

Table 1. Baseline estimates ($B, \alpha, \delta B$ and $\delta\alpha$) for the]57/173 and 157/141 pairs

Image Pair	B, In	δB, m	α, deg	$\delta\alpha$, deg
157.8 /173.8	326.9	0.55	-41.6	-0.08
157.8 /141.8	47.8	0.14	-4.5	-0.39

Table 2. Doppler centroids at C-band and I,-band of three images of the Laguna San Rafael, along with the doppler centroid used in the processor for each image pair, and the corresponding percentage of common bandwith at C-band (BW C-) and L-band (BW 1-) for each image pair. The doppler bandwith was 950 Hz at both frequencies.

Data-Take	C-band	I,-band	BW C-	BW 1,-
141.8	-680 Hz	-153 Hz		
157.8 /141.8	-588 Hz	-138 Hz	90 %	98 %
157.8	-584 Hz	-135 Hz		
1.57.8 /173.8	-374 Hz	-88 Hz	61 %	91 %
173.8	-218 Hz	-54 Hz		

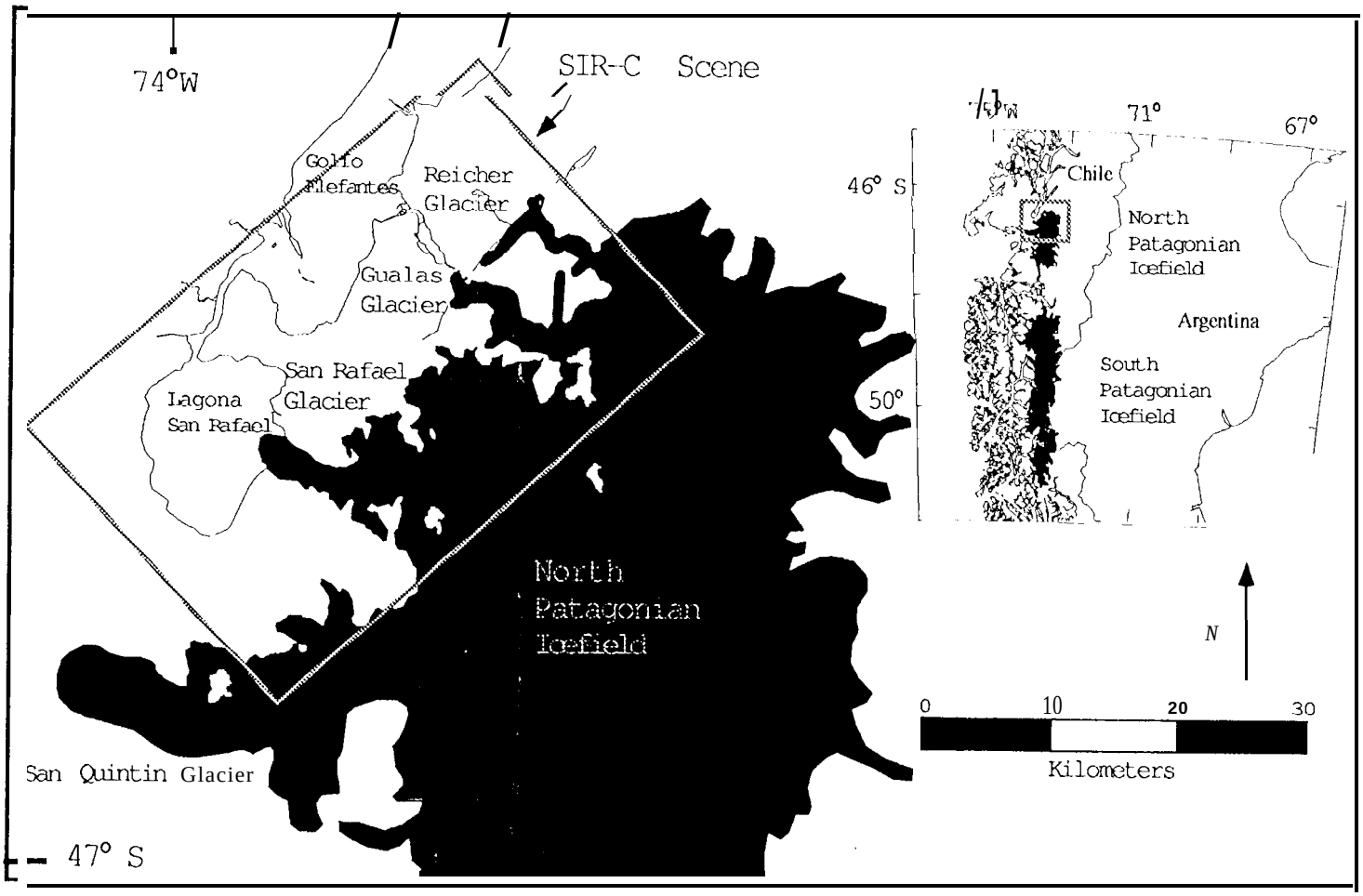
74°W
SIR-C Scene
Golfo Elefantes
Reicher Glacier
Gualas Glacier
San Rafael Glacier
Lagona San Rafael
North Patagonian Icefield
San Quintin Glacier
47° S
71°
67°
46° S
50°
Chile
North Patagonian Icefield
Argentina
South Patagonian Icefield
N
0
10
20
30
Kilometers

Figure 1.

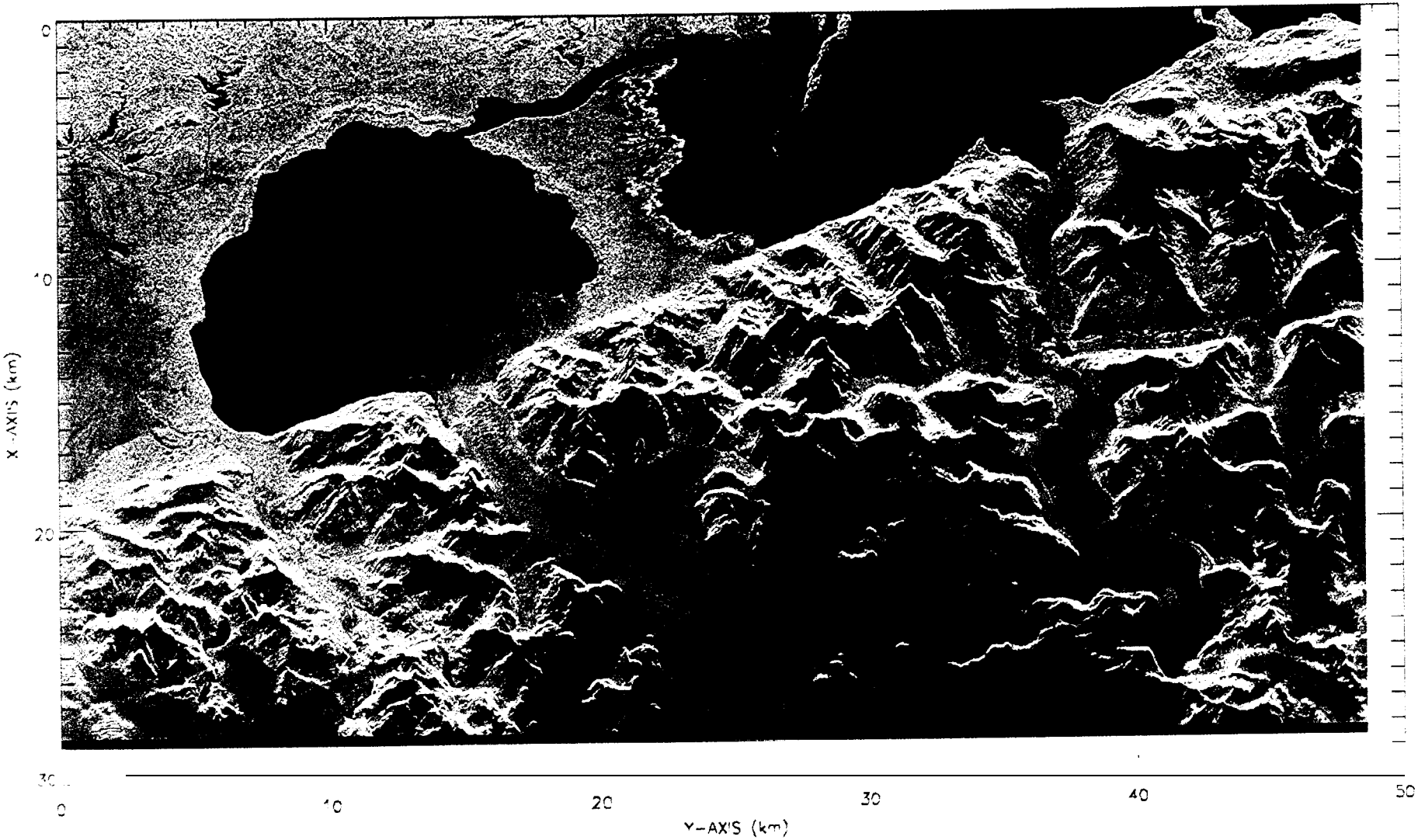

Figure 2.

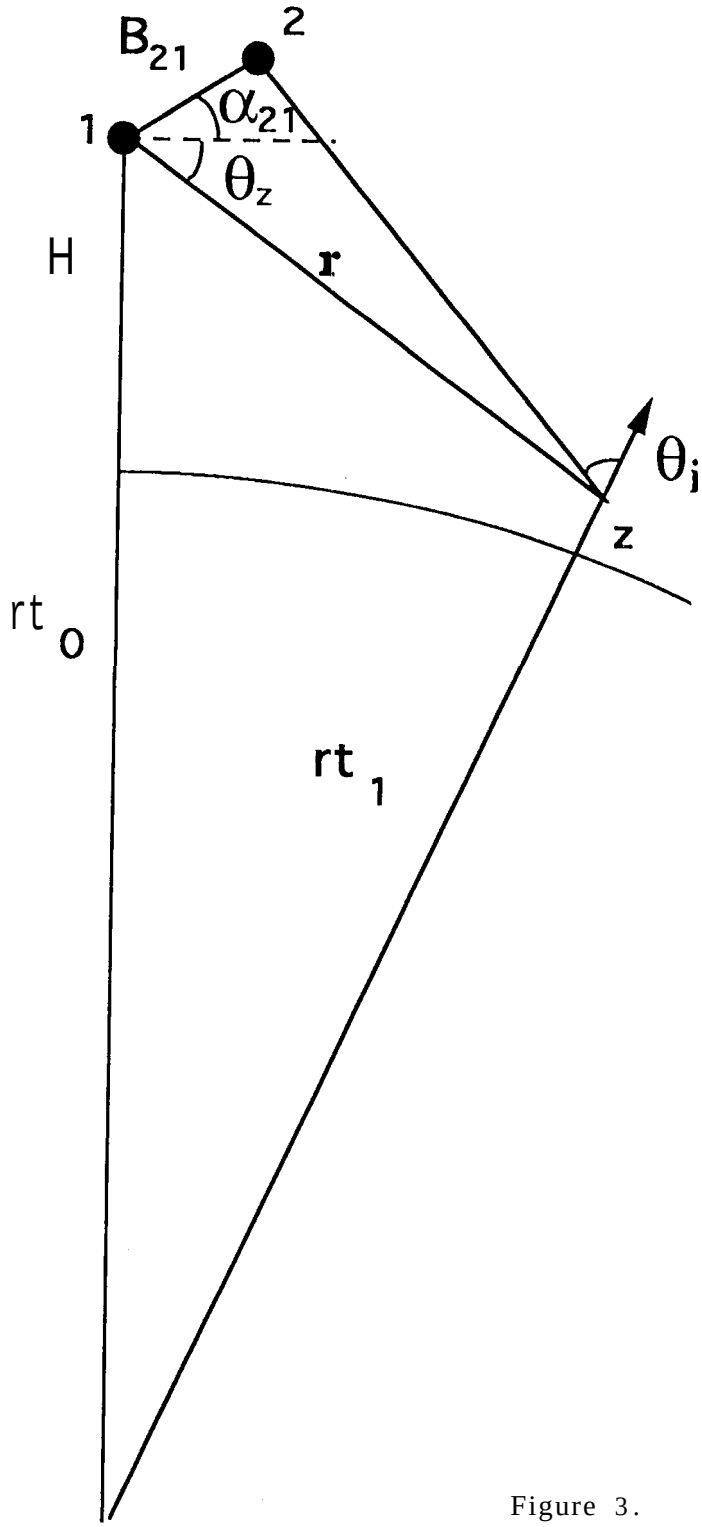

Figure 3.

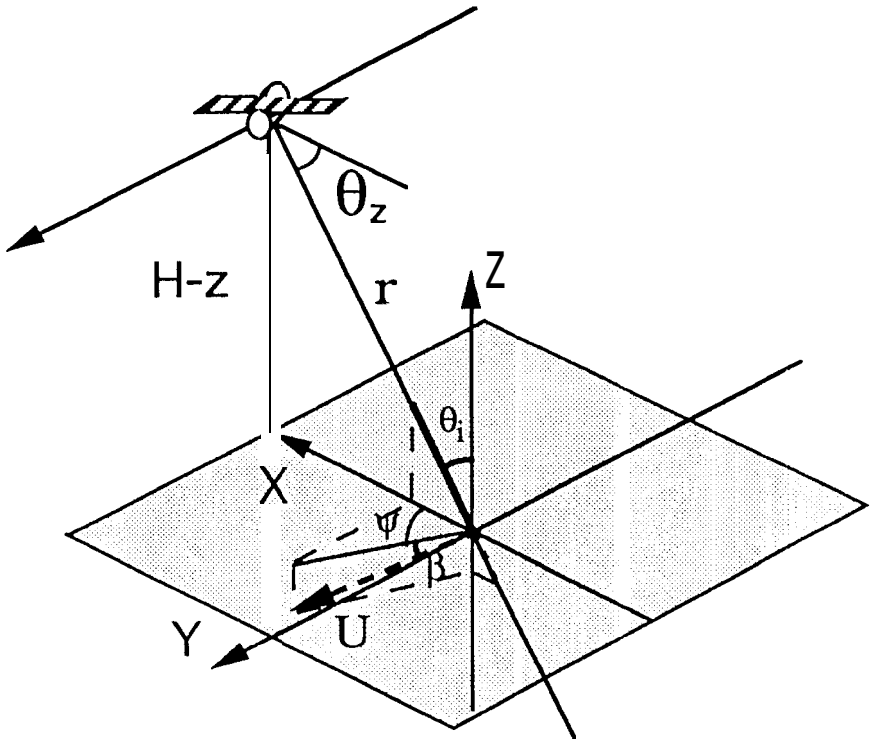

Figure 4.

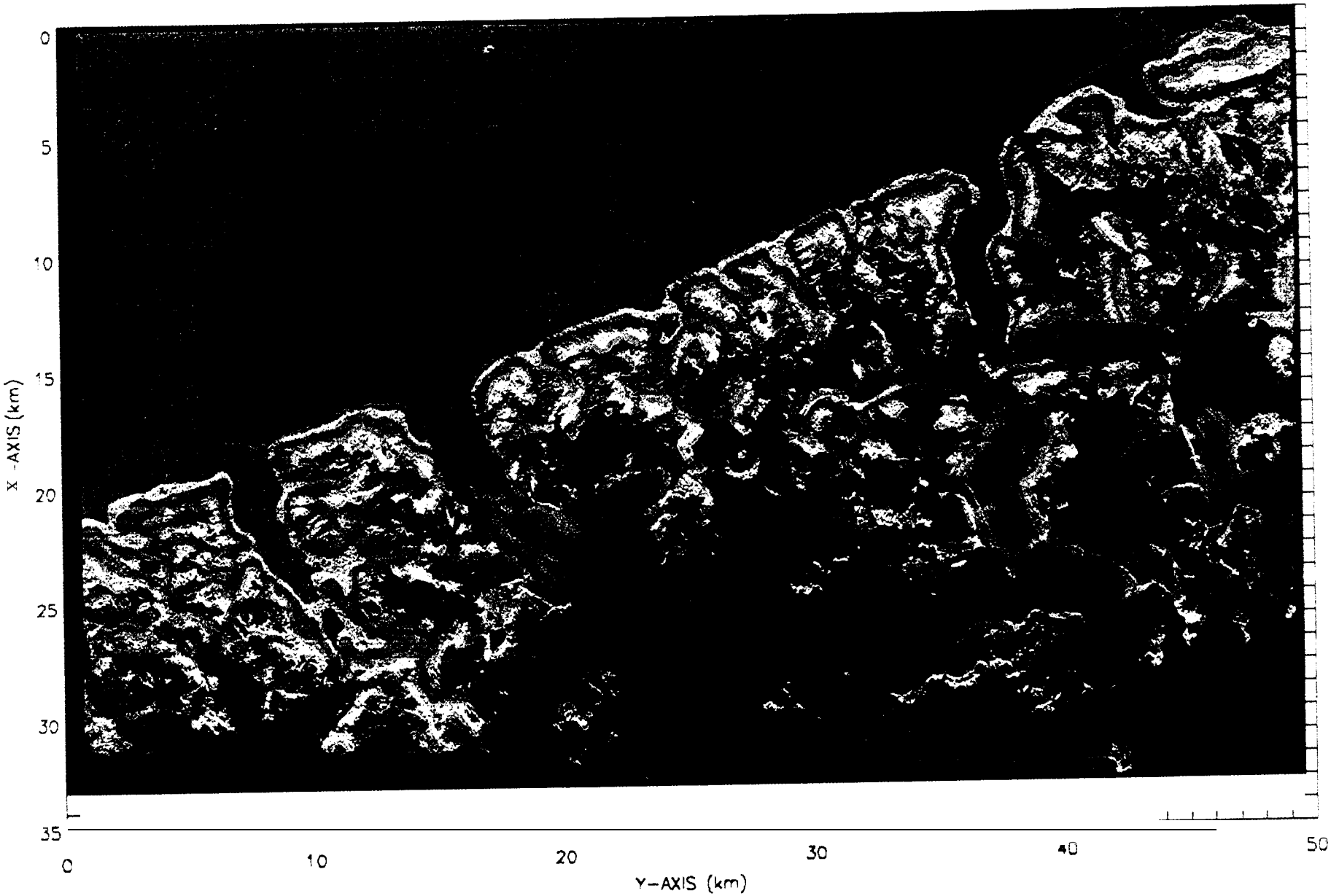

Figure 5a

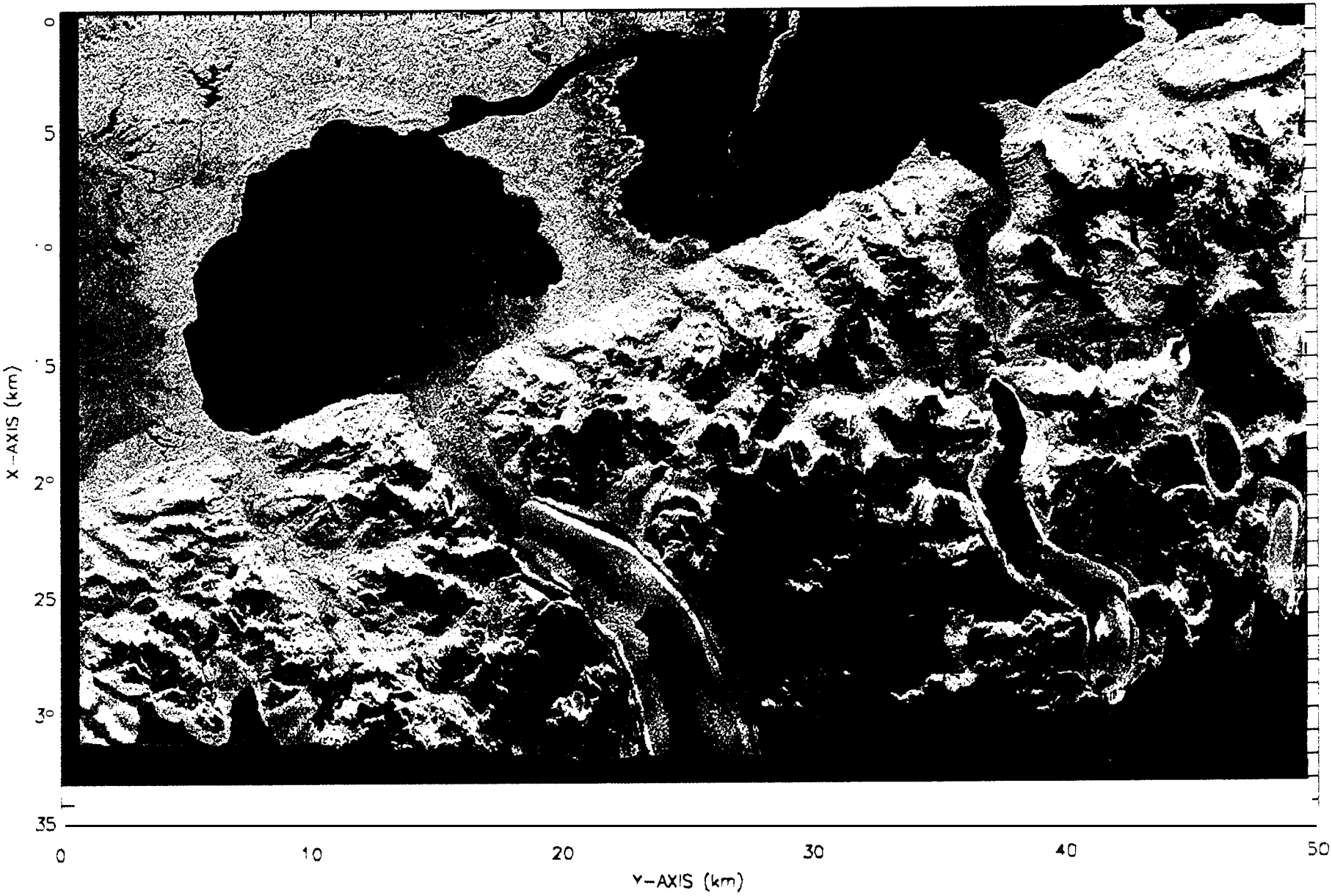

Figure 5b

a

b

Figure 6.

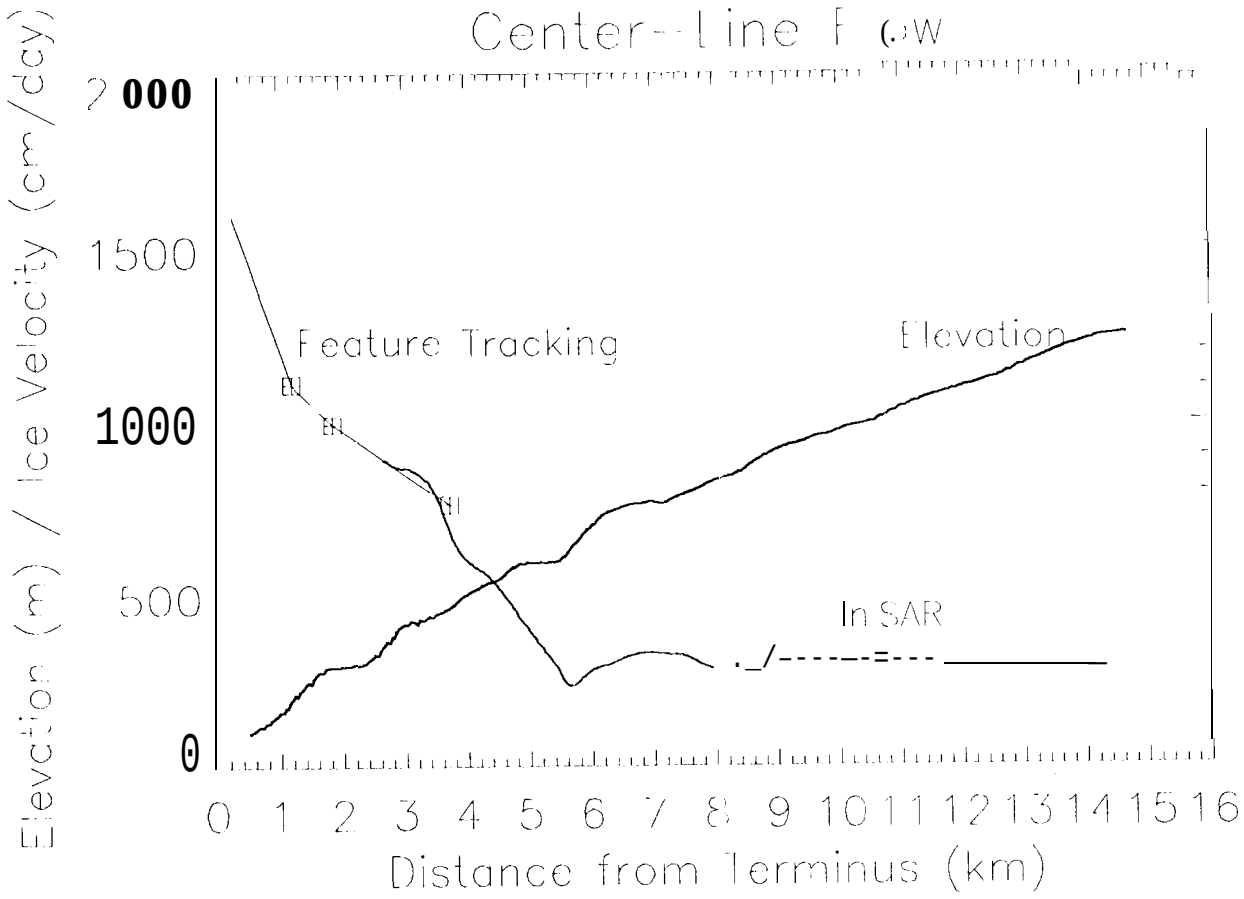
Center-Line Flow
Elevation (m) / Ice Velocity (cm/day)
2000
1500
1000
500
0
Feature Tracking
Elevation
In SAR
0 1 2 3 4 5 6 7 8 9 10 11 12 13 14 15 16
Distance from Terminus (km)

Figure 7.

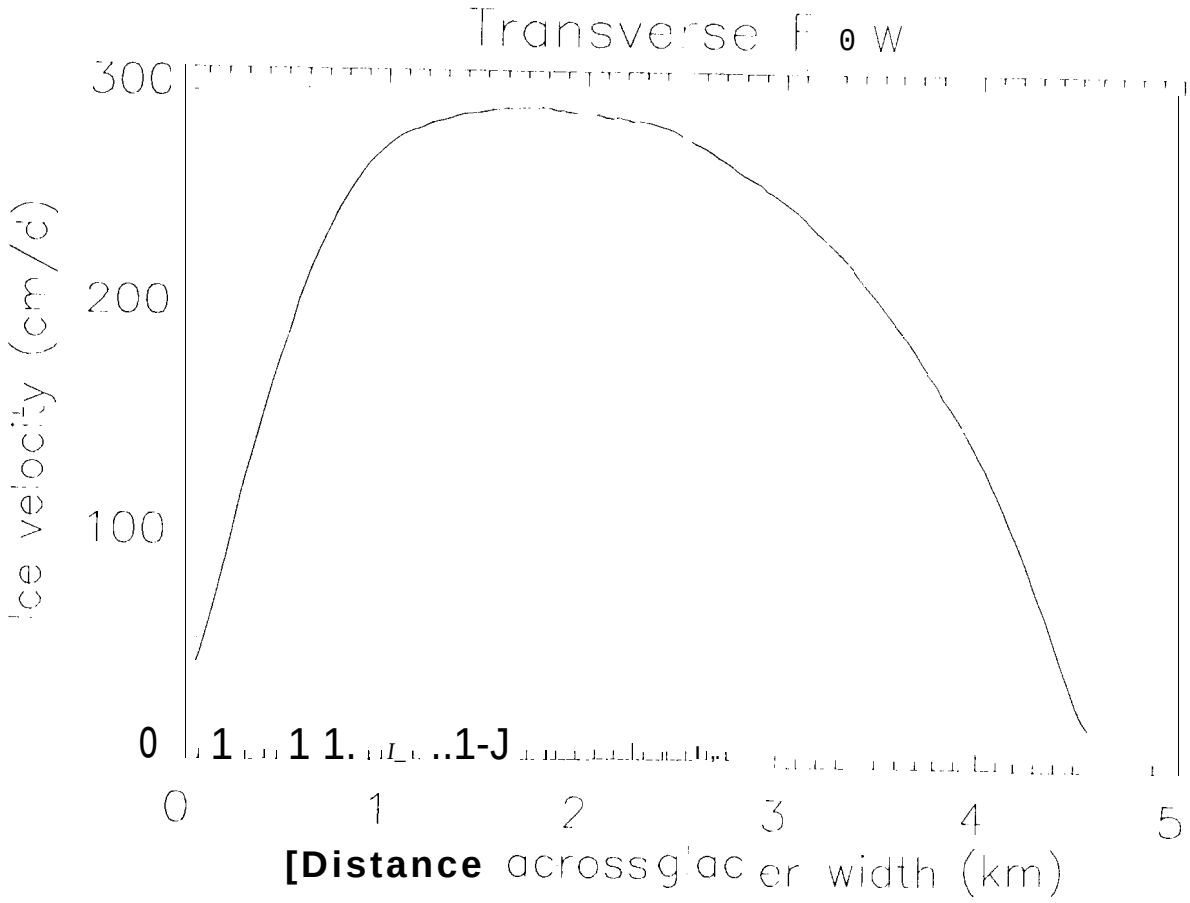
Transverse F 0 W
300
200
100
0
Ice velocity (cm/d)
0
1
2
3
4
5
[Distance across glacier width (km)

Figure 8.

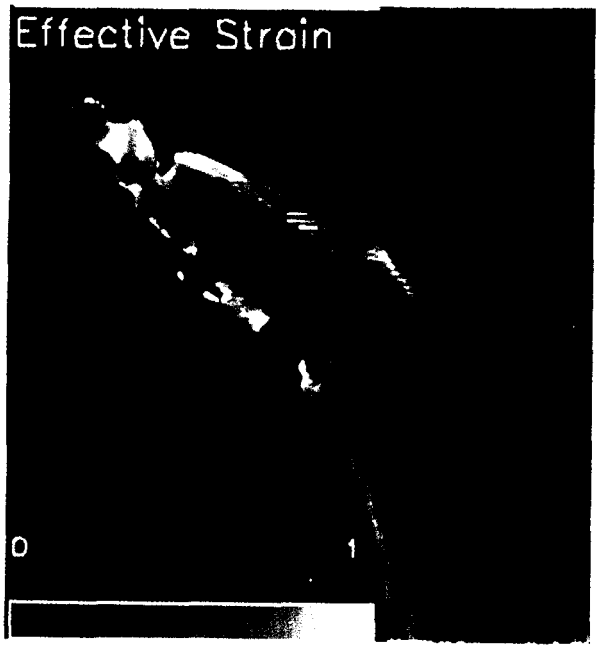

Figure 9.

Longitudinal Stress
a
-250kPa
+250kPa
Driving Stress
d
0 kPa
+250kPa
Shear Stress
b
-250kPa
+250kPa
Gradient Longitudinal Stress
e
-250kPa
+250kPa
Transverse Stress
c
-250kPa
+250kPa
Basal Drag
f
0 kPa
+250kPa

Figure 10.

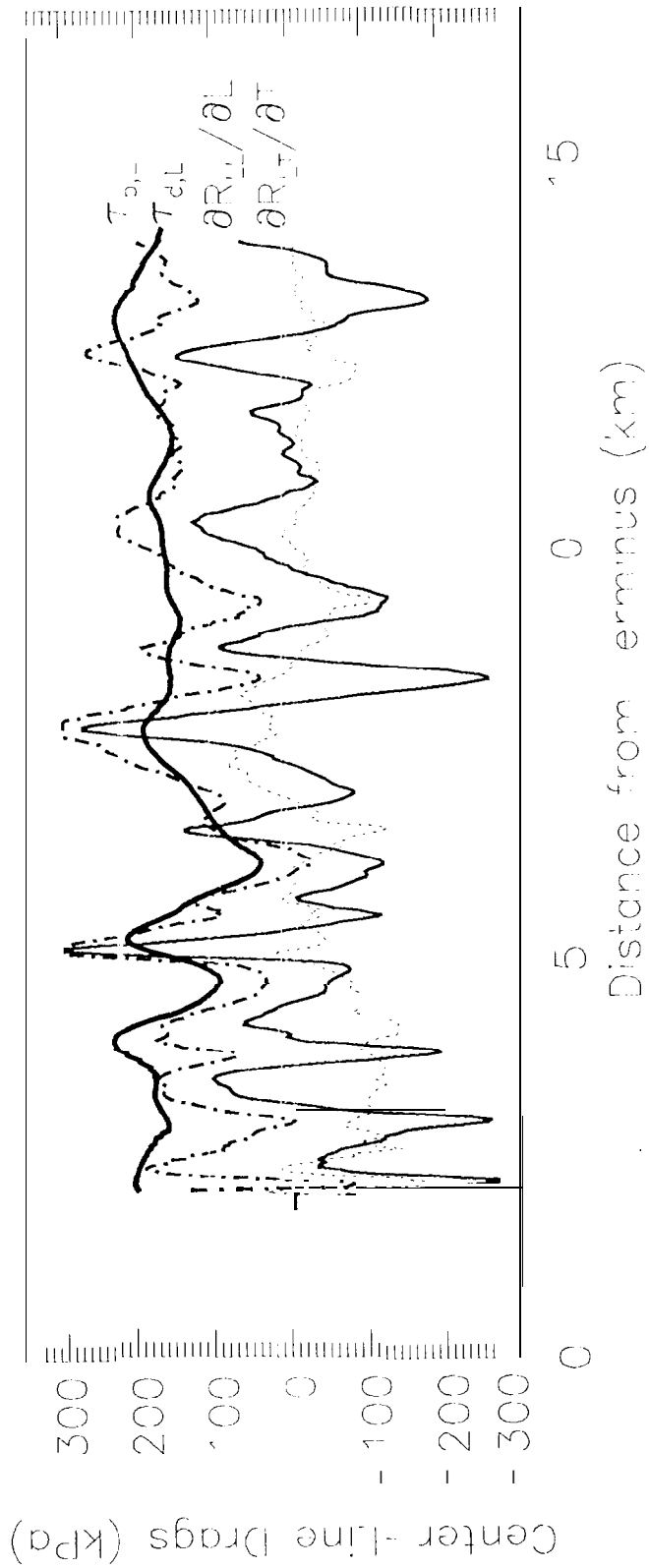
Center-line Drags (kPa)
300
200
100
0
-100
-200
-300
0
5
0
15
Distance from ermmus (km)
$\tau_{a,-}$
$\tau_{d,L}$
$\partial R_{\perp}/\partial L$
$\partial R_{\perp}/\partial T$

Figure 11.